JOURNAL OF AIRCRAFT
Vol. 38, No. 6, November–December 2001

Impulsively Started Flow About a Rigid Parachute Canopy

H. Johari*
Worcester Polytechnic Institute, Worcester, Massachusetts 01609
K. Stein†
U.S. Army Soldier and Biological Chemical Command, Natick, Massachusetts 01760
and
T. Tezduyar‡
Rice University, Houston, Texas 77005

The temporal evolution of the flowfield in the near wake of a parachute canopy is studied computationally with a finite element method. The canopy is assumed to be rigid and impermeable, and the flow is started impulsively. The separated shear layer surrounding the canopy creates a starting vortex ring. As time evolves, flow instabilities cause the vortex ring to become convoluted and eventually lead to the breakup of the ring. This phase of the flow lasts for approximately $16D/U$, where D is the mean projected diameter of the canopy and U is the freestream velocity. After the initial phase, the flow goes through a transition phase before settling into its steady state. In the steady-state phase, the drag and base pressure coefficient become nearly constant. The computed drag coefficient matches very well against experimental data. The steady-state phase is reached after a time period of approximately $45D/U$. During the steady-state phase, vortex shedding is observed in the near wake despite the nearly constant drag coefficient.

Introduction

THE long-term objective of this study is to gain a better understanding of the unsteady flow in the near wake of a parachute canopy. It is well known that the wake of bluff bodies is three-dimensional and unsteady even when the body is planar or axisymmetric. The problem becomes even more complex when the interaction between the unsteady freestream and the flexible canopy fabric is considered. To simplify the problem, the starting flow around a rigid parachute canopy is considered here. Although there are several experimental studies on rigid parachute canopy models in steady flow, there appear to be no experimental data for the starting case.

Discrete vortex methods have also been used to model the flow behind steady and transient bluff bodies.[1,2] The majority of these simulations are either planar or axisymmetric. Even though the discrete vortex methods have been used to examine the starting flow about two-dimensional bodies, such as flat and cambered plates,[3–5] to date, only few vortex method simulations have dealt with the case of parachutelike geometries. Frucht and Cockrell[6] used an axisymmetric vortex code to simulate the flow around rigid cup geometries similar to parachute canopies. Although the computed mean drag compared satisfactorily against experimental data, quasi-periodic local peaks in drag coefficient were observed. Strickland[7] developed a robust axisymmetric vortex method for the simulation of unsteady flow over parachutes. This approach resulted in favorable predictions of drag for disks, rings, and hemispherical shells in steady and transient motion as long as the flow is axisymmetric.[8] Shirayama and Kuwahara[9] devised a discrete vortex method that is capable of nonaxisymmetric simulations. However, their computed drag for a disk was underpredicted by 25%. Therefore, it appears that Navier–Stokes solvers are needed to capture accurately the three-dimensional flow in the near wake of parachute canopies.

In the present study, the impulsively started flow around a thin, rigid, impermeable canopy is computed by using a three-dimensional stabilized semidiscrete finite element formulation[10,11] of the time-dependent Navier–Stokes equations of incompressible flows. The sharp edges of this canopy geometry result in very large velocity gradients, and a stabilized formulation is needed to treat the flow in the vicinity of the canopy skirt. The evolution of the near wake from the formation of the starting vortex ring, to its breakdown, and the eventual attainment of the steady state was followed. The computed data not only illuminate the complex fluid behavior accompanying the transition from axisymmetry to three dimensionality, but also provide quantitative measures of the starting vortex ring such as its vorticity distribution. Moreover, this flow allows for the verification of the computational formulation that is used in the more sophisticated fluid–structure interaction computations in our parachute modeling effort. A byproduct of the simulation described herein is an assessment of the time needed to reach the steady state. The computational work presented here took advantage of the research code that is currently in use by the Airdrop Technology Team at the Natick Soldier Center. Further details of the computations are described in the next section.

Numerical Formulation

Governing Equations

The flow was assumed to be at a low speed, thus the Navier–Stokes equations of incompressible flows were utilized. Let $\Omega \subset R^{n_{sd}}$ and $(0, T)$ be the spatial and temporal domains, respectively, where n_{sd} is the number of space dimensions, and let Γ denote the boundary of Ω. The spatial and temporal coordinates are denoted by $\boldsymbol{x} = (x, y, z)$ and $t \in (0, T)$. The Navier–Stokes equations for incompressible flows are

$$\rho\left(\frac{\partial \boldsymbol{u}}{\partial t} + \boldsymbol{u} \cdot \nabla \boldsymbol{u} + \boldsymbol{f}\right) - \nabla \cdot \sigma = 0$$

on Ω and

$$\nabla \cdot \boldsymbol{u} = 0$$

Presented as Paper 2000-2530 at the AIAA Fluids 2000 Conference and Exhibit, Denver, CO, 19–22 June 2000; received 13 September 2000; revision received 31 July 2001; accepted for publication 27 August 2001.

*Professor, Mechanical Engineering Department. Senior Member AIAA.
†Aerospace Engineer, Airdrop Technology Team.
‡James F. Barbour Professor and Chairman, Department of Mechanical Engineering and Materials Science.

on Ω, where ρ, $\boldsymbol{u}$, $\boldsymbol{f}$, and σ are the density, velocity, body force, and stress tensor, respectively. The stress tensor for a Newtonian fluid with dynamic viscosity μ and the strain rate tensor $\varepsilon(\boldsymbol{u})$ is defined as follows:

$$\sigma(p, \boldsymbol{u}) = -p\boldsymbol{I} + 2\mu\varepsilon(\boldsymbol{u})$$

where p is pressure and $\boldsymbol{I}$ is the identity tensor.

For the flow under consideration, μ was modified locally using a Smagorinsky turbulence model[12] as follows:

$$\mu_{\text{modified}} = \mu + \rho(Ch_e)^2\sqrt{2\varepsilon:\varepsilon}$$

Here, C is a constant equal to 0.15, and h_e represents the element length scale. The variations of h_e depend on the local mesh refinement. The boundary Γ is composed of Γ_g and Γ_h, corresponding to the Dirichlet- and Neumann-type boundaries, respectively. The initial condition for the velocity is specified as $\boldsymbol{u}(\boldsymbol{x}, 0) = \boldsymbol{u}_0$ on Ω, where $\boldsymbol{u}_0$ is divergence free.

The flow solutions presented in this paper were obtained using a stabilized semidiscrete formulation for the Navier–Stokes equations (see Refs. 10 and 11). We use an unstructured mesh of linear tetrahedral elements for spatial discretization and central differencing for time integration.

Numerical Model

For the rigid canopy, the geometry of the canopy had to be fixed at the outset. The canopy geometry was derived from the finite element solution of a structural model,[13] where a constant pressure distribution was imposed on the inner face of a flat circular canopy with an effectively zero thickness. There are 24 suspension lines that limit the movement of the canopy. The resulting canopy geometry is that of the structural model after reaching static equilibrium, that is, the sum of forces being zero. The inflated canopy geometry (without the suspension lines) and the mesh used for the structural finite element solution are shown in Fig. 1. The projected diameter of the canopy, determined from the projected area $\sqrt{(4A_{\text{projected}}/\pi)}$, is equal to 70% of the original flat circular diameter. The distance between the canopy mouth and the apex is equal to 42.5% of the mean inflated diameter. Both the projected diameter and depth of the inflated canopy are within 5% of the observed values for full-scale solid cloth flat circular canopies.[14] Thus, the rigid canopy closely resembles an inflated canopy in steady descent. Henceforth, all diameters for the inflated canopy refer to the mean projected (frontal) diameter of the rigid canopy, hereafter denoted by D.

A three-dimensional tetrahedral volume mesh was generated using unstructured mesh generation software based on the strategies described by Johnson and Tezduyar.[15] The mesh surrounding the canopy is shown in Fig. 2, where the significantly increased mesh density is clearly visible from the side view. The mesh consists of 129,970 nodes and 805,797 tetrahedral elements. This mesh was selected as a result of an analogous study of an impulsively started flat disk.[16] It turns out that in the case of a disk, increasing the mesh refinement by a factor of two (from a similar number of nodes and elements) does not make any significant changes to the flow evolution or the initial or steady-state drag values. Therefore, the current mesh refinement was deemed sufficient to resolve the primary flow features in the near wake during the startup and steady-state periods. The adequacy of the mesh is further demonstrated by the close agreement between the computed drag and base pressure coefficients with the experimental data.

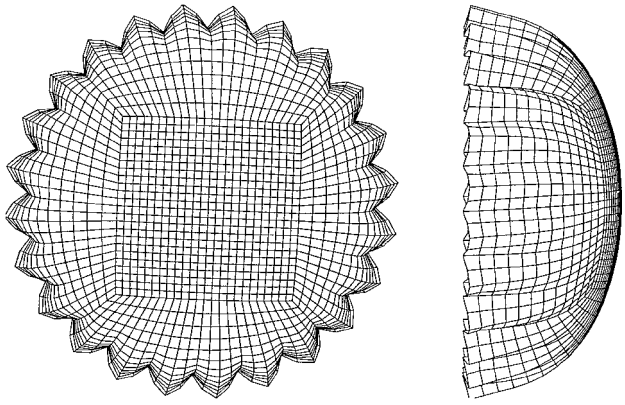

Fig. 1 Two views of the inflated rigid canopy with the structural model mesh superposed.

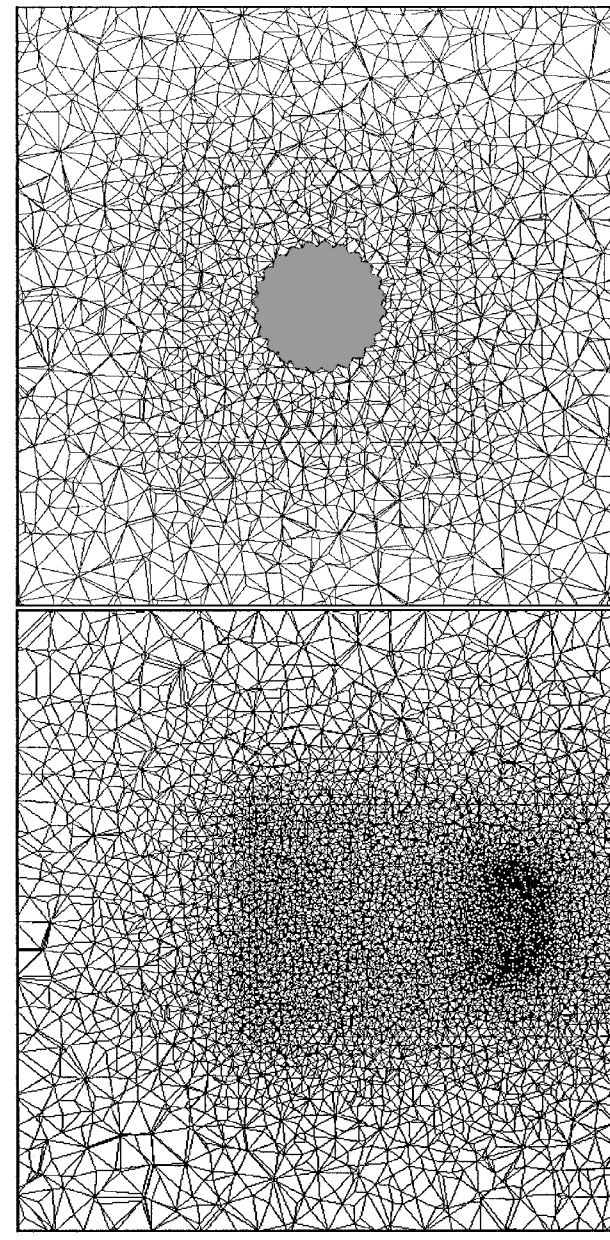

Fig. 2 End and side views of the mesh.

The computational domain consisted of a rectangular box having a square cross-section of $5.7D$ on each side and $17D$ long. The rigid canopy is located $5D$ from the inflow. A Dirichlet-type boundary condition is used at the inflow where a uniform velocity is prescribed. At the outflow, a traction-free boundary condition ($\hat{\boldsymbol{n}} \cdot \sigma = 0$, where $\hat{\boldsymbol{n}}$ is the unit normal vector) is imposed. Free-slip boundary ($\hat{\boldsymbol{n}} \cdot \boldsymbol{u} = 0$) conditions are prescribed on the four sides where the normal velocity component is set to zero. The canopy surface is treated as a no-slip boundary. The origin of the Cartesian coordinate system is placed at the mouth of the canopy, with the positive z axis (which is aligned with the symmetry axis) in the freestream direction. A mesh refinement zone covers a rectangular volume of $1.5D$ square cross section extending from $2.14D$ upstream to $7.14D$ downstream of the canopy mouth. The blockage ratio of the canopy within the computational area is 2.4%, which is comparable to a

physical model in a large wind tunnel. Thus, significant blockage effects would not be expected.

In the computations, the flow about the canopy is started impulsively at time $t = 0.0$, at a Reynolds number of 1.4×10^5. Here, the Reynolds number is based on the mean projected diameter D and the prescribed freestream velocity U. Time step sizes ranging from $0.0036D/U$ to $0.036D/U$ were employed to investigate the effects of varying the time step size. Only very minor differences were observed with different time step sizes, and the trends were identical among all cases. A time step size of $0.0143D/U$ was chosen in this study to keep the total computational time reasonable. The computations were carried out on a CRAY T3E-1200, for 5900 time steps, resulting in the flow evolution within a time period of $84.3D/U$ after the flow initiation.

Results

The development of the starting flow around a rigid parachute canopy can be divided into three phases based on the drag and flow characteristics. The first phase, which begins with the onset of simulation, is characterized by the formation, growth, and breakup of a starting vortex ring in the near-wake region. The second phase covers the transition from the starting flow to the steady-state phase. In the third phase, the flow settles in its steady state with regular vortex shedding. In this phase, the drag and the pressure at the apex of the canopy remains nearly constant in time. Velocity vectors from a cross-sectional plane during the startup and the steady-state phases are shown in Fig. 3. Although the flowfields are quite similar on the upstream side of the canopy, the flows in the near-wake region are quite different. The presence of the starting vortex ring creates a strong reverse flow within a recirculation bubble terminating at a stagnation point away from the canopy surface in the startup velocity field. On the other hand, the separated flow causes a large open wake with relatively small velocities in the steady-state regime.

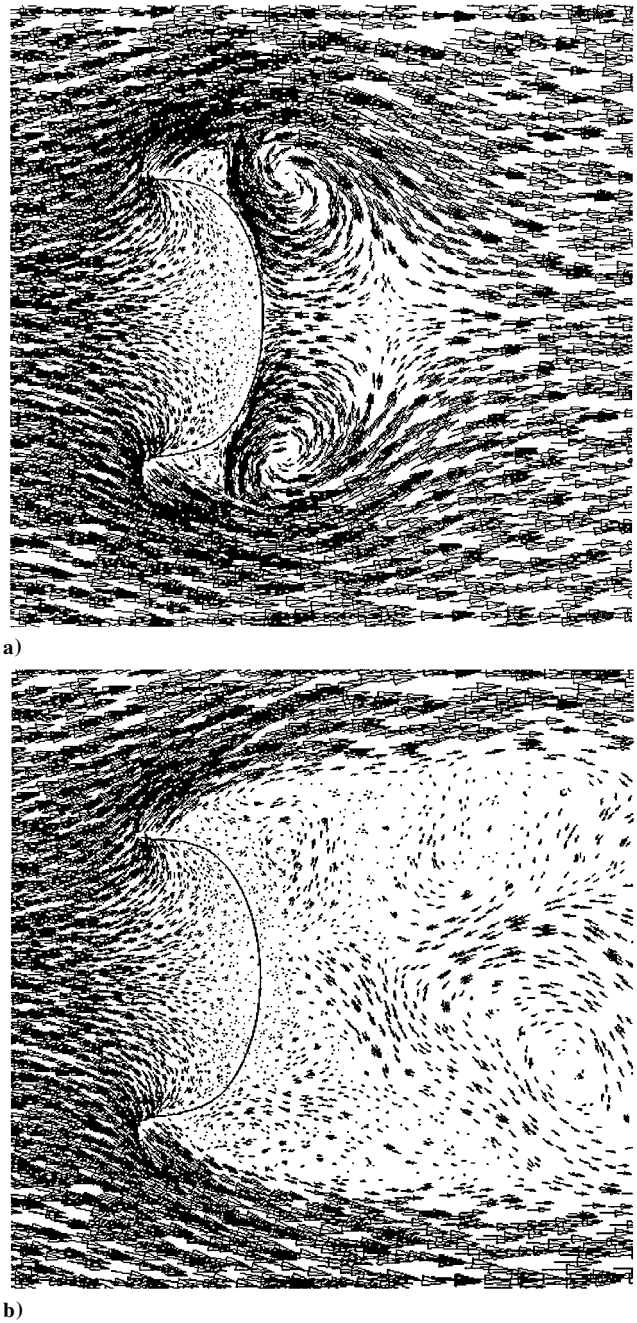

a)

b)

Fig. 3 Velocity vectors in a cross-sectional plane during the a) startup and b) steady-state phases of the flow development.

Startup Phase

A starting vortex ring rolls up in the near wake of the canopy shortly after the flow initiation. The vortex ring is axisymmetric at first and grows by the entrainment of vorticity shed from the separated shear layer formed at the perimeter of the canopy. Self-induction of the ring transports it away from the canopy. To visualize the external structure of the starting vortex ring, pressure isosurfaces are utilized. The advantage of displaying the pressure isosurfaces instead of components of the vorticity vector is the masking of the

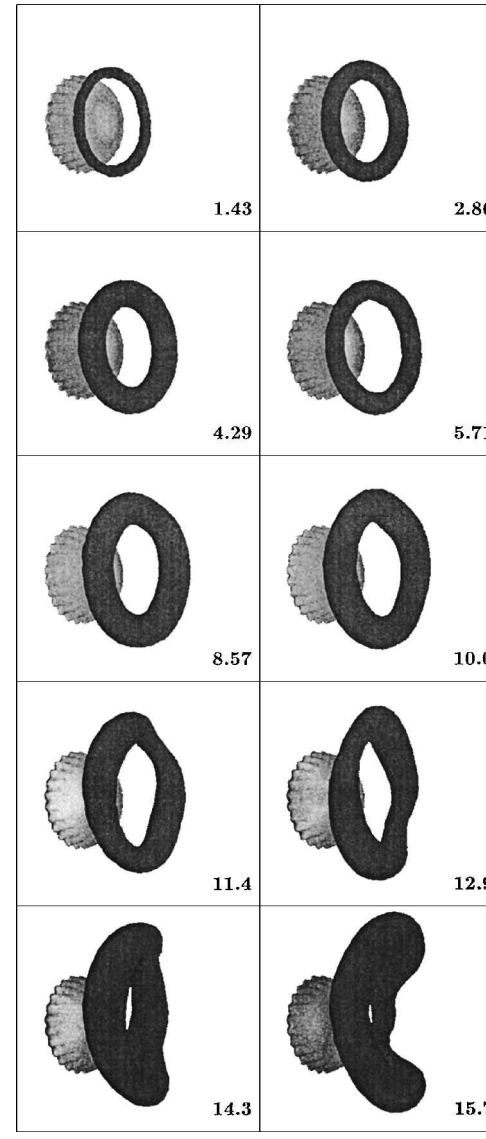

Fig. 4 Evolution of the canopy starting vortex ring as depicted by pressure isosurfaces; numbers indicate the nondimensional time.

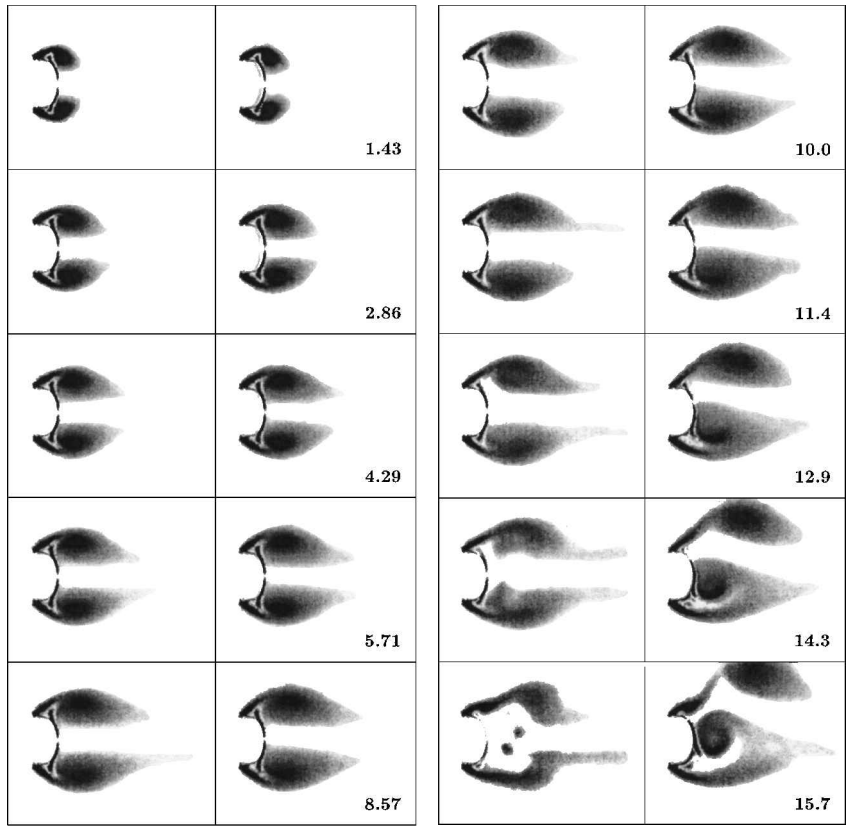

Fig. 5 Development of the azimuthal vorticity field in two perpendicular planes; numbers indicate the nondimensional time.

separated shear layer. A sequence of images in Fig. 4 reveals the evolution of the starting vortex ring depicted by pressure isosurfaces. The pressure coefficient, $C_p \equiv 2(p - p_\infty)/\rho U^2$, of the rendered surface is chosen to be −1.75, which corresponds to 93% of the minimum C_p in the vortex core at the time $1.43D/U$. The minimum pressure in the vortex core remains roughly constant (±10%), whereas the vortex ring is still symmetric. The vortex ring remains axisymmetric up to a nondimensional time of $T \equiv tU/D \approx 9$, after which the ring experiences the Widnall instability[17] and waves develop on the ring. There appear to be only a few waves on the starting ring as compared to the larger number of waves typically present on the core of free vortex rings. This is due to the thick vortex core created in the canopy wake.[17] Saffman[18] states that, in free vortex rings, the appearance and growth of the azimuthal waves is followed by a rapid localized (nonuniform in space) breakdown. We also observe that for the starting vortex ring, one side of the vortex ring moves closer to the canopy causing the vortex ring to break apart. Thereafter, complex vortex interactions ensue and the remnants of the starting vortex ring are shed at $T \approx 16$. After the onset of instability and the ensuing asymmetry, the pressure in the vortex core becomes dependent on the azimuthal position along the core.

Pressure on the rear side of the canopy is strongly affected by the starting vortex ring. Pressure at a point outside the viscous core of a vortex scales with the minimum pressure in the vortex core divided by the distance squared. Then the proximity of the ring to the canopy is directly correlated with the pressure distribution on the canopy. As will be seen, the minimum pressure in the starting vortex core remains nearly constant. Thus, as the ring moves away from the canopy, pressure on the canopy should increase with the square of the distance between the ring core and the canopy surface. The base pressure coefficient C_{pb} (i.e., at the apex of the canopy) does increase to a maximum value whereas the vortex ring retains its coherence. The highest C_p on the convex surface of the canopy remains approximately at the apex until appreciable asymmetry appears. The pressure distribution on the concave surface of the canopy remains fairly constant throughout as the starting vortex forms and then disintegrates.

The vorticity field in two perpendicular planes was extracted from the computed data to provide a different perspective of the starting vortex ring. The azimuthal component of vorticity field, which is normal to the two planes, is shown in Fig. 5. The axial and radial extent of the images is $3.5D$ in each direction. The images on the left side correspond to the azimuthal vorticity in the y–z plane whereas the images on the right side are from the x–z plane. The two planes relate to horizontal and vertical cuts in the images of Fig. 4. The darkest shades indicate the highest absolute values of azimuthal vorticity. It is evident that the vorticity field is quite axisymmetric before the image corresponding to a time of $T = 10$, consistent with the pressure surface rendering. Asymmetry of the vorticity field becomes appreciable by $T = 11.4$, where the lower portion of the vortex in the x–z plane has moved closer to the canopy surface and becomes detached from the feeding shear layer. The inward movement of the lower portion of the vortex continues until coherence of the vortex core is lost. At the same time, the upper portion of the vortex enlarges and moves further away from the canopy. These features are quite similar to those observed in the experiments of Balligand and Higuchi[19] with a starting disk (see Figs. 57 and 58 in Ref. 19). Meanwhile, the vortex core in the y–z plane has become diffuse and elongated. The azimuthal vorticity field has lost its ring structure completely in the image corresponding to $T = 12.9$. The remnants of the starting vortex ring are shed by $T \approx 16$, and smaller vortices form very close to the canopy surface. After the starting vortex is shed, streamwise vorticity filaments become prominent in the y–z plane of the wake.

Even though the vorticity distribution in the y–z plane appears to be more symmetric than that in x–z plane initially, the former also becomes asymmetric by the time the starting vortex gets shed. The appearance of instability waves create this uneven feature, which has also been observed in the development of the wake behind a sphere.[20] A recent instability analysis has shown that the most unstable mode in the steady wake of spheres and disks is helical.[21]

The development of the canopy drag C_D and base pressure coefficient C_{pb} is plotted in Fig. 6 during the first phase of the starting flow. Because of adjustment of the flow to the impulsive start,

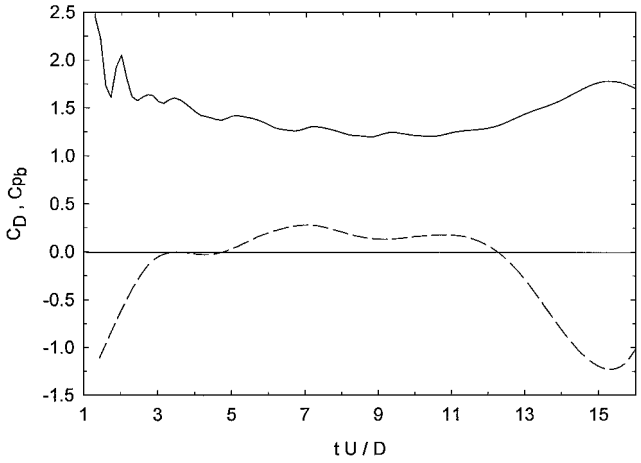

Fig. 6 Drag (——) and base pressure coefficient (– – –) during the starting phase.

the canopy drag experiences large amplitude oscillations during $0 < T < 1$. Drag decreases from a very large value (due to the impulsive start) to a minimum, whereas the base pressure increases to a maximum positive value at $T \approx 7$. As argued earlier, pressure on the canopy surface should increase with the square of the starting vortex core distance from the canopy. The pressure coefficient at the apex increases and becomes positive at $T \approx 3$ as the vortex ring moves from the immediate vicinity of the canopy. As the starting vortex ring loses its coherence, the base pressure decreases resulting in a drag increase. The observed decrease in the drag coefficient and rise in the base pressure coefficient at early times are consistent with the starting flow about a disk[16] and a two-dimensional plate.[5]

The asymmetry of the starting vortex ring after onset of the instability induces a side force on the rigid canopy. The low-pressure region associated with the portion of the vortex closest to the canopy in the x–z plane (see Figs. 4 and 5) drives the principal orientation of the side force. The side force coefficient, normalized by the dynamic pressure and the canopy projected area, along with its orientation, is shown in Fig. 7 during the startup phase of the flow. The side force coefficient increases monotonically to a peak value of 0.4 at $T = 14$ and then subsides rapidly as the starting vortex ring breaks up. The side force orientation is confined to a narrow range of angles around 180 deg, confirming the effect of the vortex ring asymmetry.

The minimum pressure in the vortex core is plotted in Fig. 8 at four azimuthal angles around the vortex. The pressure coefficient in the vortex core, which is equal to -1.9 at $T = 1.43$, experiences several oscillation cycles with an amplitude of approximately $\pm 10\%$ before the vortex ring breakup. The minimum pressure in the vortex core is nearly uniform in the azimuthal direction until $T \approx 9$, beyond which appreciable differences are observed due to the instability and eventual disintegration of the starting vortex ring. The minimum C_p in the vortex core cannot be followed sensibly beyond the time of $T \approx 16$ because of the appearance of multiple minima.

The progression of the axial and radial position of the vortex core, z_{core}/D and r_{core}/D, respectively, is shown in Fig. 9. The vortex core is found from the minimum pressure point. The axial location of the vortex is with respect to the mouth of the canopy; the apex is located at $0.425D$. The position of the vortex core at four azimuthal angles around the ring is plotted to show the initial symmetry and the subsequent loss of coherence of the vortex ring. The instability of the ring becomes apparent when the vortex core is approximately one-half of a projected diameter away from the canopy apex. The instability and subsequent breakup of the vortex ring is signified by the appreciable divergence of the vortex core location around the ring. The radial position of the starting vortex core ranges from 0.5 to $0.7D$ during the axisymmetric phase.

The peak azimuthal vorticity in the core of starting vortex ring is plotted in Fig. 10 at four azimuthal angles around the vortex. The vorticity in the shear layer rolls up into a distinct vortex core after

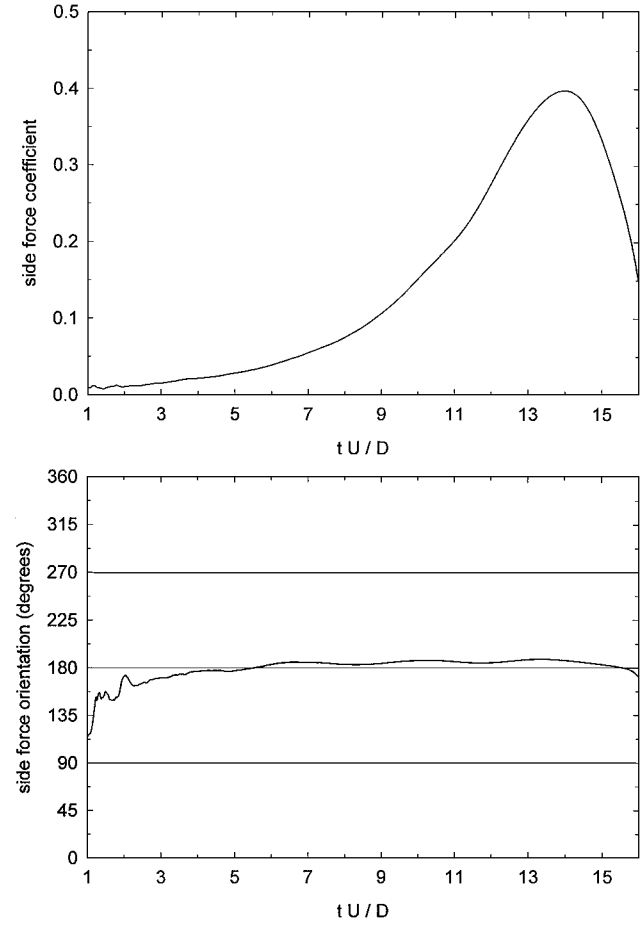

Fig. 7 Side force coefficient and its orientation during the starting phase.

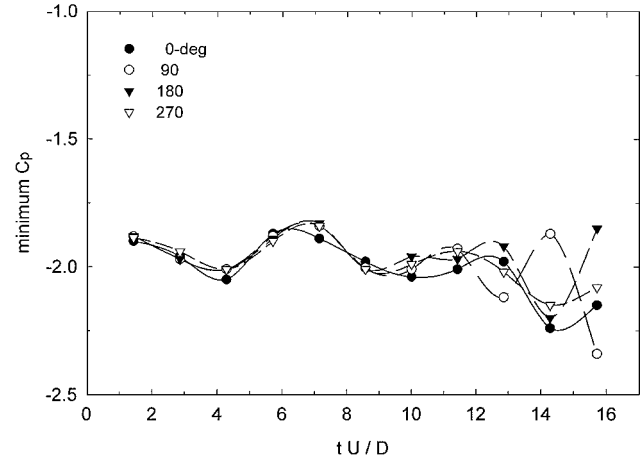

Fig. 8 Minimum pressure coefficient in the starting vortex core at four azimuthal angles.

a time of $T = 0.5$. The azimuthal vorticity decreases continuously while the starting vortex ring is axisymmetric. The decrease is due to the diffusion of vorticity as the vortex expands. The close agreement of the vorticity values at different angles before the ring instability further indicates the symmetry of the vortex. The divergence of the peak vorticity values around the ring starts at $T \approx 10$, in excellent agreement with the data in the minimum C_p plot of Fig. 8. The axial and radial locations of the maximum azimuthal vorticity, which provide the trajectory of the vortex core, are quite similar to those obtained from the minimum pressure location in Fig. 9.

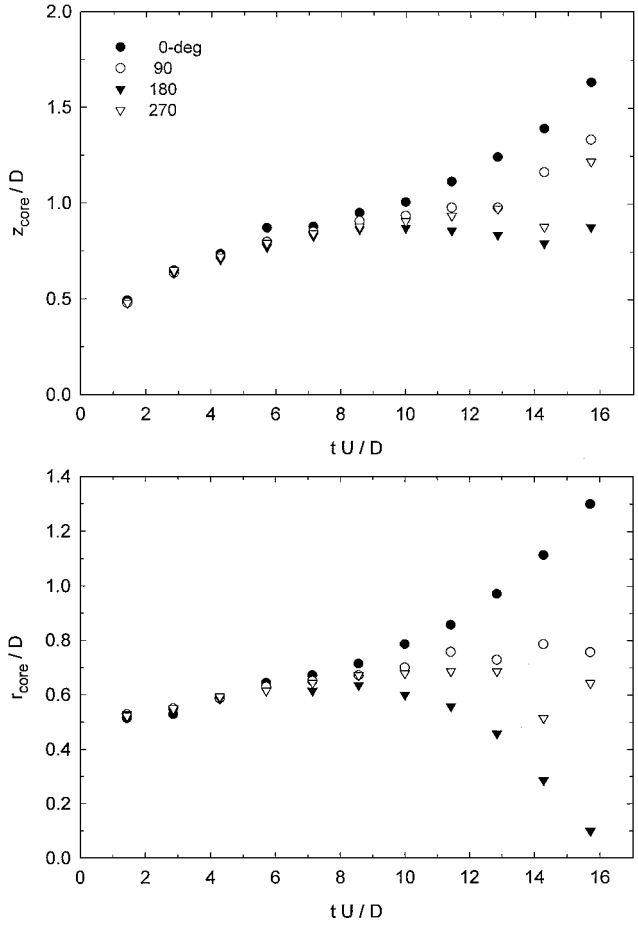

Fig. 9 Axial and radial position of the starting vortex core derived from the minimum pressure.

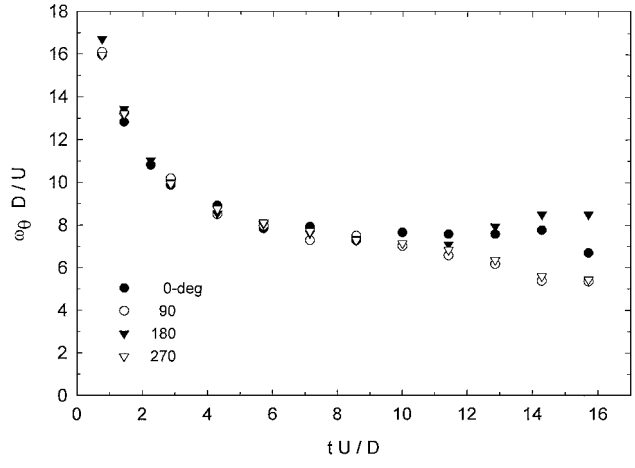

Fig. 10 Maximum azimuthal vorticity in the core of the starting vortex ring.

Because of the symmetry of the vortex ring in the azimuthal direction before the onset of instabilities, the mean vortex core trajectory can be found from either the vorticity or pressure field. The mean vortex core trajectory is plotted in Fig. 11 from the initial rollup to the time of $T = 10$. The canopy contour along a radial is also shown in this Fig. 11. The data from the pressure and vorticity fields correspond to the same time instants during the development of the wake. The vortex core positions from the minimum pressure appear to be inward and slightly further downstream of those from the peak azimuthal vorticity. Also note that the vortex core moves almost solely in the downstream direction up to a time of $T \approx 2$, before expanding in the radial direction.

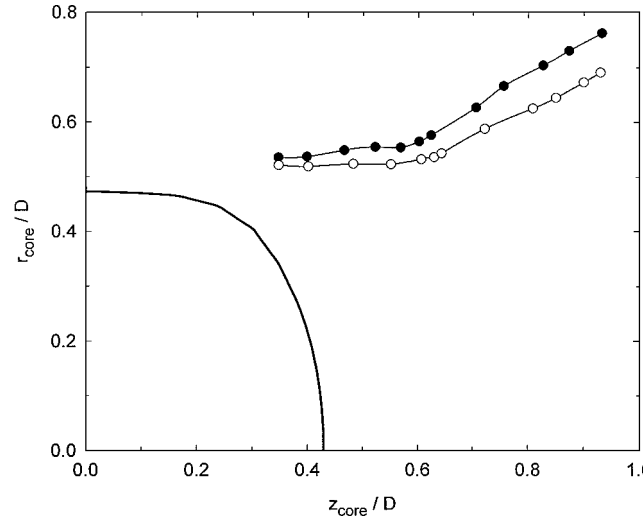

Fig. 11 Mean trajectory of the vortex core during the axisymmetric period: filled symbols ● indicate the data derived from the maximum vorticity and open symbols ○ the data from minimum pressure; canopy outline along a radial is also drawn on the plot.

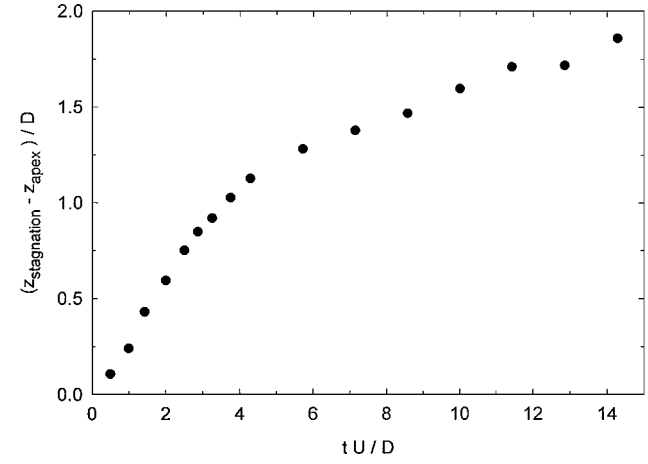

Fig. 12 Location of the stagnation point in the near wake during the starting phase.

A consequence of the presence of the starting vortex ring in the starting phase is the formation of a recirculation bubble with a stagnation point away from the canopy surface. The off-surface stagnation point is clearly discernible in the symmetric flowfield of Fig. 3a. As the starting vortex ring evolves, the bubble enlarges, and the stagnation point moves farther away from the canopy. The stagnation point remains on the symmetry axis until a time of $T \approx 13$, after which it moves away from the z axis and disappears shortly after $T \approx 14$. The latter time corresponds with the loss of ring coherence. The motion of the stagnation point is shown in Fig. 12, where the distance between the canopy apex and the stagnation point is plotted. The stagnation point moves about $1.5D$ away from the apex while the flow is still symmetric. It moves another $0.5D$ farther before vanishing. The breakup of the starting vortex ring and the ensuing three-dimensional flowfield is the cause of the stagnation point disappearance.

Steady-State Phase

The evolution of the flowfield following the initial phase is marked by a transition phase before the flow settles in its steady state. The computed drag and base pressure coefficient history for the entire computational period are shown in Figs. 13 and 14, respectively. During the transition phase, the drag coefficient increases to a maximum value of 2.33 at $T = 18.5$ before leveling off at a plateau at

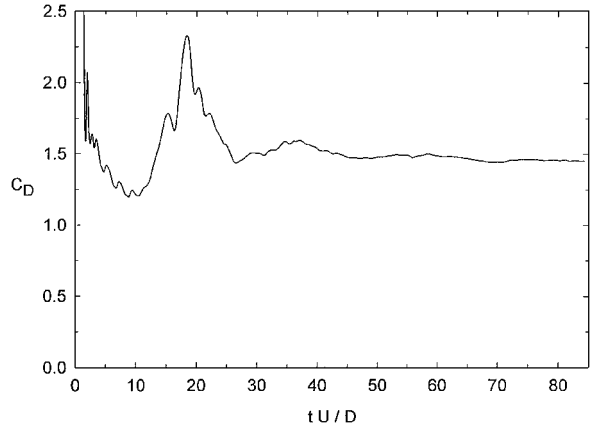

Fig. 13 Drag coefficient history.

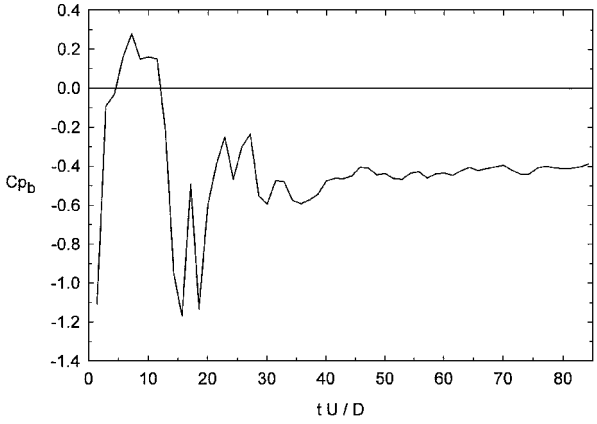

Fig. 14 Time history of the base pressure coefficient.

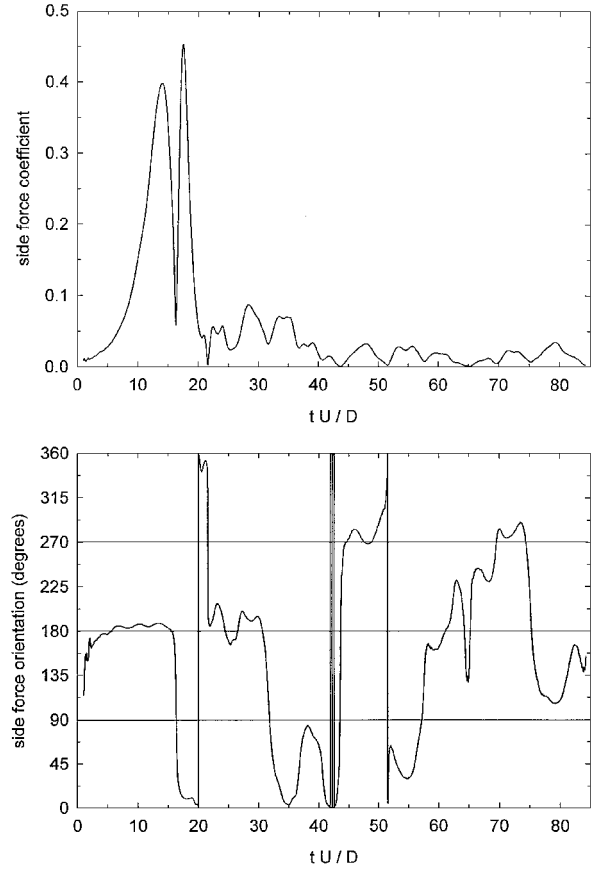

Fig. 15 Time history of the side force coefficient and its orientation.

1.47 ± 0.02. The drag coefficient is nearly constant for times greater than about $T = 45$. The steady-state drag coefficient is within 5% of the published data for a rigid canopy in uniform flow.[22] The agreement between the published data and the steady-state drag becomes even better when the latter is corrected for blockage, using the standard blockage correction schemes. The base pressure coefficient has a maximum at $T \approx 7$ and a minimum at $T \approx 15$. The base pressure coefficient settles in its steady-state value of -0.43 ± 0.02 for times greater than $T = 50$. This value of the steady-state base pressure coefficient is quite close to the commonly accepted value of -0.45 for rigid bluff bodies such as cups and disks.

The side force coefficient for the entire simulation period is plotted in Fig. 15 along with its orientation. The initial peak in the side force coefficient, due to the asymmetry of the starting vortex ring, is followed by a second peak during the transition phase at a time $T \approx 17.5$. This peak force is due to the formation of a small-scale vortex tube very close to the canopy. The position of this vortex tube matches the side force orientation during the second peak. Also, the latter peak occurs nearly at the same time as when the peak in the drag coefficient is observed. The maximum side force is about 20%

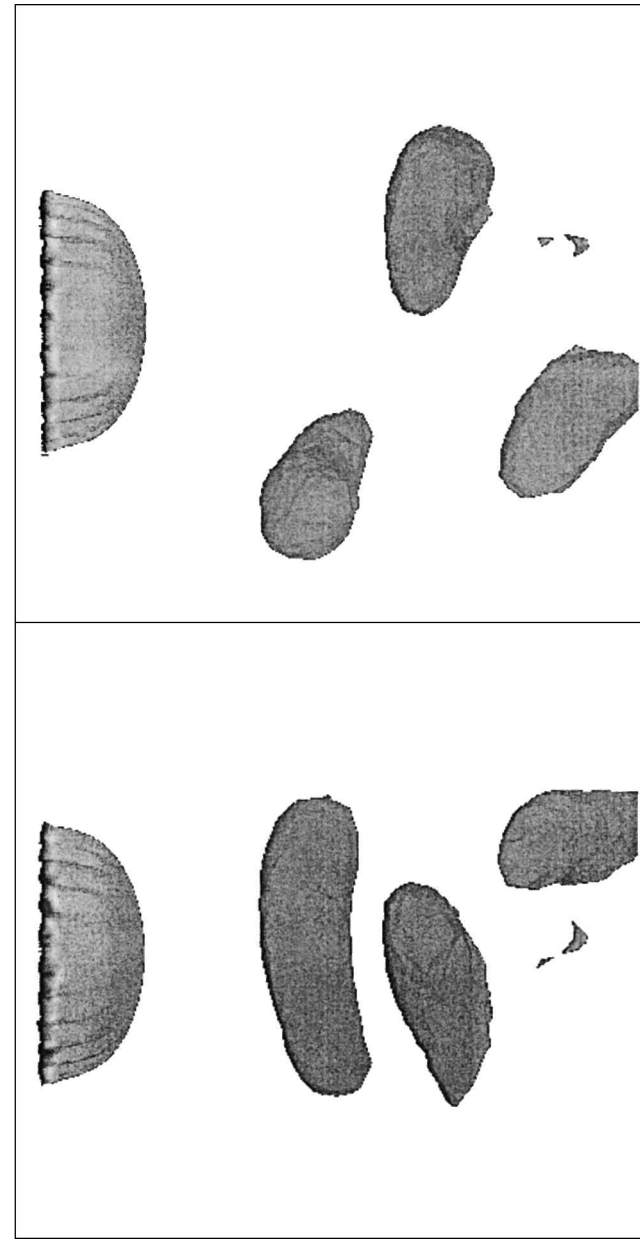

Fig. 16 Two views of the vortex shedding pattern as revealed by constant pressure surfaces at a time of $T = 77$.

of the drag. As the flow settles into its steady state, the side force coefficient approaches a nearly constant value of 0.016 ± 0.009 for times greater than $T = 45$. This value is about 1% of the mean drag coefficient. The orientation of the side force changes from the 180-deg value during the startup phase to a range covering the entire 360-deg domain during the steady state. The sharp vertical lines in the plot are due to the crossing of the angle from 0 to 360 deg and vice versa.

The nearly constant canopy drag during the steady-state phase of the flow brings into question whether vortex shedding was captured in the computations. To answer this question, constant pressure surfaces in the near wake of the canopy at time $T = 77$ are rendered in Fig. 16. Two nearly perpendicular side views of the fluid volumes having pressure coefficients less than -0.6 are shown in Fig. 16. The geometry of these surfaces indicates crescent-shaped patterns for vortex tubes shed from the canopy at quasi-regular intervals. The lack of streamwise vortex filaments in Fig. 16 is due to the visualization scheme that masks weaker vorticity filaments and the separating shear layer.

Conclusions

One of the most valuable findings of this study was that the stabilized semi-discrete finite element formulation utilized here is clearly able to compute the unsteady flowfield accurately even in the presence of sharp edges and creases associated with an effectively zero thickness parachute canopy model. Most grid-based formulations cannot handle the very large velocity gradients near the canopy lip. The close matching of the mean drag and base pressure coefficient during the steady state is an indicator of the accuracy of the aforementioned formulation.

Furthermore, there are several remarkable observations regarding the starting flow in the near wake of a rigid canopy. A surprisingly long time of $45D/U$ is needed for drag to settle into the steady-state value. Similarly long times to reach steady state were observed in the experiments of Chua et al.[5] for the case of a starting two-dimensional flat plate and in the computations of a solid disk.[16] Another observation concerning drag is the existence of the dip at $T \approx 9$. Again, similar minima have been observed for disks and flat plates. The distribution of vorticity in the starting vortex is quite axisymmetric at $T \approx 1$ despite the highly convoluted shear layer feeding the vortex. Apparently, the azimuthal modulation of the canopy lip, visible in Fig. 1, does not appreciably affect the starting vortex ring symmetry. Although the reasons for this observation are not clear, we suspect that viscosity (real or artificial) has smoothed the creases in the feeding shear layer.

In conclusion, the flowfield in the near wake of a rigid, impermeable parachute canopy is studied computationally for an impulsively started flow condition utilizing a three-dimensional finite element formulation. The separating shear layer surrounding the canopy rolls up into a symmetric starting vortex ring. As time evolves, the vortex ring moves away from the canopy, and its diameter increases. A Widnall-type instability causes the vortex ring to become wavy and convoluted. This leads to the breakup of the starting vortex. Complex vortex interactions follow, and the remnants of the starting vortex ring are shed. This phase of the flow takes about $16D/U$.

After the initial phase, the flow goes through a transition phase, where the drag reaches a local peak before settling into its steady state at a time of $45D/U$. In the steady-state phase, the drag and base pressure coefficients remain nearly constant. The computed steady-state drag coefficient matches very well against available experimental values. Vortex shedding in the form of crescent-shaped filaments is observed despite the relatively constant drag coefficient in the steady-state phase.

Acknowledgments

This work was supported by the Natick Soldier Center (NSC) under the auspices of the U.S. Army Research Office Scientific Services program administered by Battelle (Delivery Order 437, Contract DAAH04-96-C-0086). The encouragement of Richard Benney and Calvin Lee during the first author's visit to the Airdrop Technology Team at NSC is appreciated.

References

[1] Sarpkaya, T., "An Inviscid Model of Two-Dimensional Vortex Shedding for Transient and Asymptotically Steady Separated Flow over an Inclined Plate," *Journal of Fluid Mechanics*, Vol. 68, Pt. 1, 1975, pp. 109–128.

[2] Kiya, M., and Arie, M., "A Contribution to an Inviscid Vortex-Shedding Model for an Inclined Flat Plate in Uniform Flow," *Journal of Fluid Mechanics*, Vol. 82, Pt. 2, 1977, pp. 223–240.

[3] Sarpkaya, T., and Kline, H. K., "Impulsively Started Flow About Four Types of Bluff Bodies," *Journal of Fluids Engineering*, Vol. 104, No. 2, 1982, pp. 207–213.

[4] Sarpkaya, T., Mostafa, S. M., and Munz, P. D., "Numerical Simulation of Unsteady Flow About Cambered Plates," *Journal of Aircraft*, Vol. 27, No. 1, 1990, pp. 51–59.

[5] Chua, K., Lisoski, D., Leonard, A., and Roshko, A., "A Numerical and Experimental Investigation of Separated Flow Past an Oscillating Flat Plate," *ASME International Symposium on Nonsteady Fluid Dynamics*, FED-Vol. 92, American Society of Mechanical Engineers, Fairfield, NJ, 1990, pp. 455–464.

[6] Frucht, Y. I., and Cockrell, D. J., "A Discrete Free Vortex Method of Analysis for Inviscid Axisymmetric Flows Around Parachute Canopies," AIAA Paper 91-0850, June 1991.

[7] Strickland, J. H., "Prediction Method for Unsteady Axisymmetric Flow over Parachutes," *Journal of Aircraft*, Vol. 31, No. 3, 1994, pp. 637–643.

[8] Higuchi, H., Balligand, H., and Strickland, J. H., "Numerical and Experimental Investigations of the Flow over a Disk Undergoing Unsteady Motion," *Journal of Fluids and Structures*, Vol. 10, 1996, pp. 705–719.

[9] Shirayama, S., and Kuwahara, K., "Computation of Flow Past a Parachute by a Three-Dimensional Vortex Method," AIAA Paper 86-0350, Jan. 1986.

[10] Tezduyar, T. E., "Stabilized Finite Element Formulations for Incompressible Flow Computations," *Advances in Applied Mechanics*, Vol. 28, 1991, pp. 1–44.

[11] Tezduyar, T. E., and Osawa, Y., "Methods for Parallel Computation of Complex Flow Problems," *Parallel Computing*, Vol. 25, 1999, pp. 2039–2066.

[12] Smagorinsky, J., "General Circulation Experiments with the Primitive Equations," *Monthly Weather Review*, Vol. 91, 1963, pp. 99–165.

[13] Benney, R., Stein, K., Zhang, W., Accorsi, M. L., and Leonard, J. W., "Controllable Airdrop Simulations Utilizing a Three-Dimensional Structural Dynamic Model," AIAA Paper 99-1727, June 1999.

[14] Knacke, T. W., *Parachute Recovery Systems Design Manual*, Para Publishing, Santa Barbara, CA, 1992, p. 5-3.

[15] Johnson, A. A., and Tezduyar, T. E., "Parallel Computation of Incompressible Flows with Complex Geometries," *International Journal for Numerical Methods in Fluids*, Vol. 24, 1997, pp. 1321–1340.

[16] Johari, H., and Stein, K., "Temporal Evolution of the Wake of an Impulsively Started Disk," *Proceedings of the 2000 ASME Fluids Engineering Summer Conference*, FEDSM2000-11170, American Society of Mechanical Engineers, Fairfield, NJ, 2000.

[17] Widnall, S. E., "The Structure and Dynamics of Vortex Filaments," *Annual Reviews of Fluid Mechanics*, Vol. 7, 1975, pp. 141–165.

[18] Saffman, P. G., "The Number of Waves on Unstable Vortex Rings," *Journal of Fluid Mechanics*, Vol. 84, Pt. 4, 1978, pp. 625–639.

[19] Balligand, H., and Higuchi, H., "Experimental Investigation of the Wake Behind a Solid Disk," Sandia National Labs. Rept. SAND 90-7083, Albuquerque, NM, Dec. 1993.

[20] Shirayama, S., "Flow Past a Sphere: Topological Transitions of the Vorticity Field," *AIAA Journal*, Vol. 30, No. 2, 1992, pp. 349–358.

[21] Natarjan, R., and Acrivos, A., "The Instability of the Steady Flow Past Spheres and Disks," *Journal of Fluid Mechanics*, Vol. 254, 1993, pp. 323–344.

[22] Hoerner, S. F., *Fluid-Dynamic Drag*, published by the author, Midland Park, NJ, 1965, pp. 3–17.